Biosensors and Bioelectronics 238 (2023) 115561

Contents lists available at ScienceDirect

Biosensors and Bioelectronics

journal homepage: www.elsevier.com/locate/bios

Discriminating macromolecular interactions based on an impedimetric fingerprint supported by multivariate data analysis for rapid and label-free *Escherichia coli* recognition in human urine

Adrian Koterwa [a,1], Mattia Pierpaoli [b,1], Bożena Nejman-Faleńczyk [c], Sylwia Bloch [c], Artur Zieliński [d], Wioletta Adamus-Białek [e], Zofia Jeleniewska [f], Bartosz Trzaskowski [g], Robert Bogdanowicz [b], Grzegorz Węgrzyn [c], Paweł Niedziałkowski [a,**], Jacek Ryl [f,*]

[a] Department of Analytical Chemistry, Faculty of Chemistry, University of Gdańsk, Wita Stwosza 63, 80-308, Gdańsk, Poland
[b] Department of Metrology and Optoelectronics, Gdańsk University of Technology, Narutowicza 11/12, 80-233, Gdańsk, Poland
[c] Department of Molecular Biology, Faculty of Biology, University of Gdansk, Wita Stwosza 59, 80-308, Poland
[d] Faculty of Chemistry, Gdańsk University of Technology, Narutowicza 11/12, 80-233, Gdańsk, Poland
[e] Institute of Medical Sciences, Jan Kochanowski University of Kielce, IX Wieków Kielc 19A, 25-317, Kielce, Poland
[f] Division of Electrochemistry and Surface Physical Chemistry, Faculty of Applied Physics and Mathematics, Gdańsk University of Technology, Narutowicza 11/12, Gdańsk, 80-233, Poland
[g] Centre of New Technologies, University of Warsaw, Banach 2c, 02-097, Warsaw, Poland

ARTICLE INFO

Keywords:
Multiparametric impedance discriminant analysis
E. coli
Electrochemical biosensor
Human urine analysis

ABSTRACT

This manuscript presents a novel approach to address the challenges of electrode fouling and highly complex electrode nanoarchitecture, which are primary concerns for biosensors operating in real environments. The proposed approach utilizes multiparametric impedance discriminant analysis (MIDA) to obtain a fingerprint of the macromolecular interactions on flat glassy carbon surfaces, achieved through self-organized, drop-cast, receptor-functionalized Au nanocube (AuNC) patterns. Real-time monitoring is combined with singular value decomposition and partial least squares discriminant analysis, which enables selective identification of the analyte from raw impedance data, without the use of electric equivalent circuits. As a proof-of-concept, the authors demonstrate the ability to detect *Escherichia coli* in real human urine using an aptamer-based biosensor that targets RNA polymerase. This is significant, as uropathogenic *E. coli* is a difficult-to-treat pathogen that is responsible for the majority of hospital-acquired urinary tract infection cases. The proposed approach offers a limit of detection of 11.3 CFU/mL for the uropathogenic *E. coli* strain No. 57, an analytical range in all studied concentrations (up to 10^5 CFU/mL), without the use of antifouling strategies, yet not being specific vs other *E.coli* strain studied (BL21(DE3)). The MIDA approach allowed to identify negative overpotentials (−0.35 to −0.10 V vs Ag/AgCl) as most suitable for the analysis, offering over 80% sensitivity and accuracy, and the measurement was carried out in just 2 min. Moreover, this approach is scalable and can be applied to other biosensor platforms.

1. Introduction

Developing an electrochemical biosensing platform that is both industrially scalable and repeatable is a challenging task that requires meeting various requirements. To achieve low limits of detection (LOD) and selectivity, many available technologies rely on complex synthetic

* Corresponding author.
** Corresponding author.
E-mail addresses: adrian.koterwa@phdstud.ug.edu.pl (A. Koterwa), mattia.pierpaoli@pg.edu.pl (M. Pierpaoli), bozena.nejman-falenczyk@ug.edu.pl (B. Nejman-Faleńczyk), sylwia.bloch@ug.edu.pl (S. Bloch), artur.zielinski@pg.edu.pl (A. Zieliński), wioletta.adamus-bialek@ujk.edu.pl (W. Adamus-Białek), s185379@student.pg.edu.pl (Z. Jeleniewska), b.trzaskowski@cent.uw.edu.pl (B. Trzaskowski), r.bogdanowicz@eti.pg.edu.pl (R. Bogdanowicz), grzegorz.wegrzyn@ug.edu.pl (G. Węgrzyn), pawel.niedzialkowski@ug.edu.pl (P. Niedziałkowski), jacek.ryl@pg.edu.pl (J. Ryl).
[1] these authors contributed equally to this work.

https://doi.org/10.1016/j.bios.2023.115561
Received 12 May 2023; Received in revised form 29 July 2023; Accepted 31 July 2023
Available online 1 August 2023
0956-5663/© 2023 The Authors. Published by Elsevier B.V. This is an open access article under the CC BY license (http://creativecommons.org/licenses/by/4.0/).

methods and nanoarchitecture designs, difficult to control when expanding production, thus leading to sub-ideal structural features or loss in their special, surface-related functions (Chen et al., 2022; Sharifi et al., 2019). Additionally, the ability to develop platforms with high sensitivity and selectivity in complex biological samples is of paramount importance (Russo et al., 2021). Popular strategies to reduce fouling are through nanoengineered surfaces (Chapman et al., 2015; Zhou et al., 2009) or the application of nanoporous membranes (Sun et al., 2016), which further increase the complexity and reduce the reproducibility and scale-up potential of the proposed approaches. Another strategy includes developing antifouling coatings to prevent the non-specific molecules adsorption. Here, single-molecule fouling agents after receptor grafting (Niedzialkowski et al., 2020), molecular brushes (Emilsson et al., 2015), zwitterionic coatings (Gui et al., 2013), but also supramolecular hydrogels (Wu et al., 2017) should be considered.

Owing to the high surface area-to-volume ratio and unique electronic and catalytic properties, gold nanoparticles are excellent candidates for enhancing the sensitivity and selectivity of electrochemical biosensors (Xiao et al., 2020). Gold nanocubes (AuNCs) have recently gained particular attention due to their uniform dimensions, higher self-organization predictability, and the ability to finely tune their plasmonic properties, as well as chemical stability (Park et al., 2018). The molecular mechanism of AuNC assembly essentially depends on the electrode substrate, strongly affecting the resultant electrocatalytic effect. Among commonly utilized electrode substrates, AuNCs decorated at GC provide over 65% increase in electrochemically active surface area and 75% increase in heterogeneous rate constant (Niedzialkowski et al., 2022). Voltammetry aptasensors based on AuNCs were used for the determination of chloramphenicol (LOD = 2.8 pM) (Lu et al., 2021), progesterone in diluted blood (LOD = 1 ng/mL) (Velayudham et al., 2021) and even a prostate cancer gene sequence (10 nM), also exhibiting low disturbance in the presence of fouling agents (Abedi et al., 2021). DNA biosensors for pathogenic *Vibrio cholerae*, responsive even at quantities of 10 CFU/mL, and selective detection in bacterial cultures belonging to the same and distant genera (Ali et al., 2021). Moreover, surface modification of AuNC makes it possible to produce a signal-enhanced interface, such as in the case of the paper-based chikungunya virus platform built based on magnetic Fe_3O_4@AuNC (Singhal et al., 2018), or the hollow Ag@AuNC core-shell for surface-enhanced Raman scattering and non-enzymatic uric acid and ascorbic acid detection (Bhattacharjee et al., 2020).

Human urine is a product of the filtration system – the kidneys – and was conventionally considered as sterile (Kass, 1962). Even though the results of next generation sequencing analyses provide evidence of the existence of the urine microbiome, there are still many controversial aspects to this topic (Frimodt-Møller, 2019; Grine et al., 2019; Shah Utsav et al., 2021) and the common belief is that urine in the bladder of a healthy person is not contaminated with bacteria. However, bacteria can enter the urinary system, causing problems such as infection and inflammation. Urinary tract infection (UTI) is considered the second most common bacterial disease after pneumonia and affects about 150 million people every year worldwide (Flores-Mireles et al., 2015). Annually, UTIs are diagnosed in more than 10% of women and 3% of men, and more than 60% of women will be diagnosed with a UTI in their lifetime (Klein and Hultgren, 2020). The clinical picture of the UTI ranges from a mild self-limiting illness, chronic or acute infection, to urosepsis. Additionally, urosepsis comprises 25% of all adult sepsis cases and is associated with an overall mortality rate of 20–40%. Primary hospitalized patients due to UTIs result in a total cost of $2.8 billion USD in the United States, annually; epidemiological reports also indicate 1 million visits to the emergency department and 7 million office visits (Klein and Hultgren, 2020). Uropathogenic *Escherichia coli* (UPEC) is the most common pathogen, responsible for 85% and 50% of community and hospital-acquired UTI cases, respectively, and can form biofilms on urological catheters, making them very difficult to treat and remove due to the high tolerance of biofilm structures to antibiotics.

The standard urine culture protocol represents the primary tool for detecting bacteria in clinical microbiology laboratories with LOD > 10^5 CFU/mL (Kass, 1962; Price et al., 2016). Dipsticks and culturing methods take long time (hours, even days), limiting rapid intervention. In turn, the use of some molecular methods as polymerase chain reaction (PCR) could improve the speed and accuracy of UPEC detection; however, their applicability is complicated by the high genomic variability within uropathogenic *E. coli* strains (Brons et al., 2020). Other diagnostic technologies for UTIs are also known, i.e. urinalysis and microscopy, fluorescent *in situ* hybridization (FISH), MALDI-TOF MS, microfluidics, immunology-based and forward light scattering assays; however, their limiting factors, described recently in detail (Davenport et al., 2017), prevent their use in clinics. A powerful approach to the detection of *E. coli* via electrochemical biosensors is by immunosensors (Felix and Angnes, 2018). Many electrode modifications were performed to obtain as low limits of detection (LOD) as possible, such as photochemical immobilization of anti-*E. coli* antibodies on gold (Cimafonte et al., 2020), gold modified by graphene-wrapped copper (II)-assisted cysteine hierarchical structure, and antibodies (Pandey et al., 2017). Wang et al. show a 10 CFU/mL LOD with composite biosensors based on magnetic nanoparticles (NPs) and functionalized gold nanoparticles (AuNPs) conjugated with lead sulfide NPs via oligonucleotide linkage (R. R. Wang et al., 2015; Y. Y. Wang et al., 2015). Another route to use immuno-functionalized magnetic beads is by glucose oxidase (GOx)–antibody conjugates at interdigitated microelectrodes (10^3 CFU/mL) (Xu et al., 2016). A bionanocomposite based on pencil graphite modified with chitosan, multiwalled carbon nanotubes, polypyrrole and AuNPs offers a LOD of 30 CFU/mL (Güner et al., 2017). The utilization of nucleic acid hybridization or connection to DNA is also used in *E. coli* biosensors. The gold electrode modified by thiolated capture probes and biotinylated aptamer probes had an 80 CFU/mL E. *coli* LOD (Wang et al., 2019). Limits of detection under 10 CFU/mL were obtained with biosensors based on metal–organic frameworks functionalized by polyaniline at glassy carbon electrode (GCE) (Shahrokhian and Ranjbar, 2018) and indium-tin oxide (ITO) modified by 3-Aminopropyltrimethoxysilane and DNA genetic markers (Deshmukh et al., 2020).

Detecting analytes in real human urine poses significant challenges due to the potential for unknown interactions to occur between the biosensor surface, the analyte, and other molecules present in the sample (Aitekenov et al., 2021). As a result, only a limited number of studies have proposed electrochemical methods for detecting analytes in urine. Typically, detection in urine is based on the use of antibody-modified electrodes, and the measurements focus on the clinical utility of the biosensors that have been designed. Such examples include a GCE functionalized by a nanocomposite of polyaniline with AuNPs and MoS_2 modified by antibodies or Au modified with thin reduced graphene oxide and polyethylenimine (Jijie et al., 2018), both with LODs of 10 to 10^5 CFU/mL (Raj et al., 2021). The screen-printed carbon electrode with an AuNP-decorated polyaniline film and anti-digoxigenin-labeled horseradish peroxidase was manifested to detect 4 to 4×10^6 CFU/mL *E. coli* in urine (Shoaie et al., 2018). However, despite the efforts, achieving uniform PANI distribution and volume for scale-up remains a critical challenge (Yang et al., 2023), while quantitative analysis is required in specific sensing scenarios.

In this work, we have developed a novel approach to the detection of large biomolecules using modulated electrostatic interactions induced by electrode polarization, mitigating common biofouling and indirect readout. Simultaneous biosystem perturbations by a package of multiple pre-selected frequency signals was analyzed by the Singular Value Decomposition (SVD) followed by Partial Least Squares Discriminant Analysis (PLS-DA) to effectively discriminate the signal response in the presence or absence of the target molecule. Such a strategy delivers an explicit impedimetric fingerprint of the macromolecular interactions, which is dependent not only on binding moieties but also coulombic interactions at different charge states at the electrode surface. We have demonstrated the functionality of the proposed proof-of-concept at an

MOST WIEDZY Downloaded from mostwiedzy.pl

aptamer-based biosensor composed of self-organized Au nanocube patterns at a flat glassy carbon electrode, applied for the rapid detection of *E. coli* in real human urine samples through polymerase RNA. Importantly, the measured impedance values were directly used for the analyses, avoiding errors that may accumulate during the standard fitting procedures with electric equivalent circuits.

2. Experimental

2.1. Chemicals and bacteria strains used

All chemicals were of analytical grade and were used as purchased without further purifications. Plates of glassy carbon electrode (GCE), 12x12x3 mm, SIGRADUR G, were purchased from (HTW Hochtemperatur-Werkstoffe GmbH, Germany). All electrochemical measurements were carried out in vessels containing a circular seal with a radius of 7 mm. AuNCs were obtained according to the procedure previously described in the paper (Niedzialkowski et al., 2022), see detailed instruction in the **SI file**, **section 1**. The AuNCs were stored in a 1 mM cetyltrimethylammonium bromide (CTAB) solution.

The *E. coli* RNA polymerase holoenzyme (RNAP) used in this study, composed of the core enzyme and sigma factor 70, was obtained from the New England Biolabs company (cat No. M0551S). Both strands of the strong $p_{rrnG\text{-}P1}$ promoter – nontemplate (coding) strand with -10 and -35 motifs indicated in bold: 5′-CGA TAA AGT TTT TAT ATT TTT CGC **TTG TCA** GGC CGG AAT AAC TCC C**TA TAA T**GC GCC ACC A-3′, and template (noncoding) strand: 5′-TGG TGG CGC ATT ATA GGG AGT TAT TCC GGC CTG ACA AGC GAA AAA TAT AAA AAC TTT ATC G-3' – were synthesized by Genomed SA. The nontemplate strand was also modified at its 5′ end using thiol linker: 5′-SH-$(CH_2)_6$-CGA TAA AGT TTT TAT ATT TTT CGC TTG TCA GGC CGG AAT AAC TCC CTA TAA TGC GCC ACC A-3'. The RNAP holoenzyme is solely capable of unwinding the dsDNA helix (Bae et al., 2015; Glyde et al., 2017).

The nonpathogenic *E. coli* B strain BL21(DE3) (Clock et al., 2008) (EC-B) was obtained from the collection of the Department of Molecular Biology of the University of Gdańsk (Poland). The uropathogenic *E. coli* strain No. 57 (UPEC-57) was identified in the urine of a 14-year-old male patient from the Nephrology Clinic and donated with an antibiogram for research from the Department of Microbiology of the Regional Hospital in Kielce, Poland, in 2017. All liquid bacterial cultures were grown in Luria-Bertani medium (LB; EPRO, Poland) with aeration at 37 °C in a shaking incubator (200 RPM). Details on bacterial strain growth and suspension preparation are given in the **SI file, section S2**. The Petri dishes with LB solid medium with 1.5% bacteriological agar (LA; BTL Company, Poland) were incubated at 37 °C for approximately 18 h.

2.2. Biosensor electrode modification

All GCEs were cleaned with a polishing cloth and 0.03 μm aluminum oxide powder (Buehler, USA) before use. AuNCs dissolved in a 0.001 M CTAB solution were deposited onto the GCE surface using a 10 μL drop casting method (see SEM micrograph in Fig. 1b). The solution was allowed to dry on the electrode surface for 30 min at room temperature, then the electrodes were washed with warm water to remove the CTAB

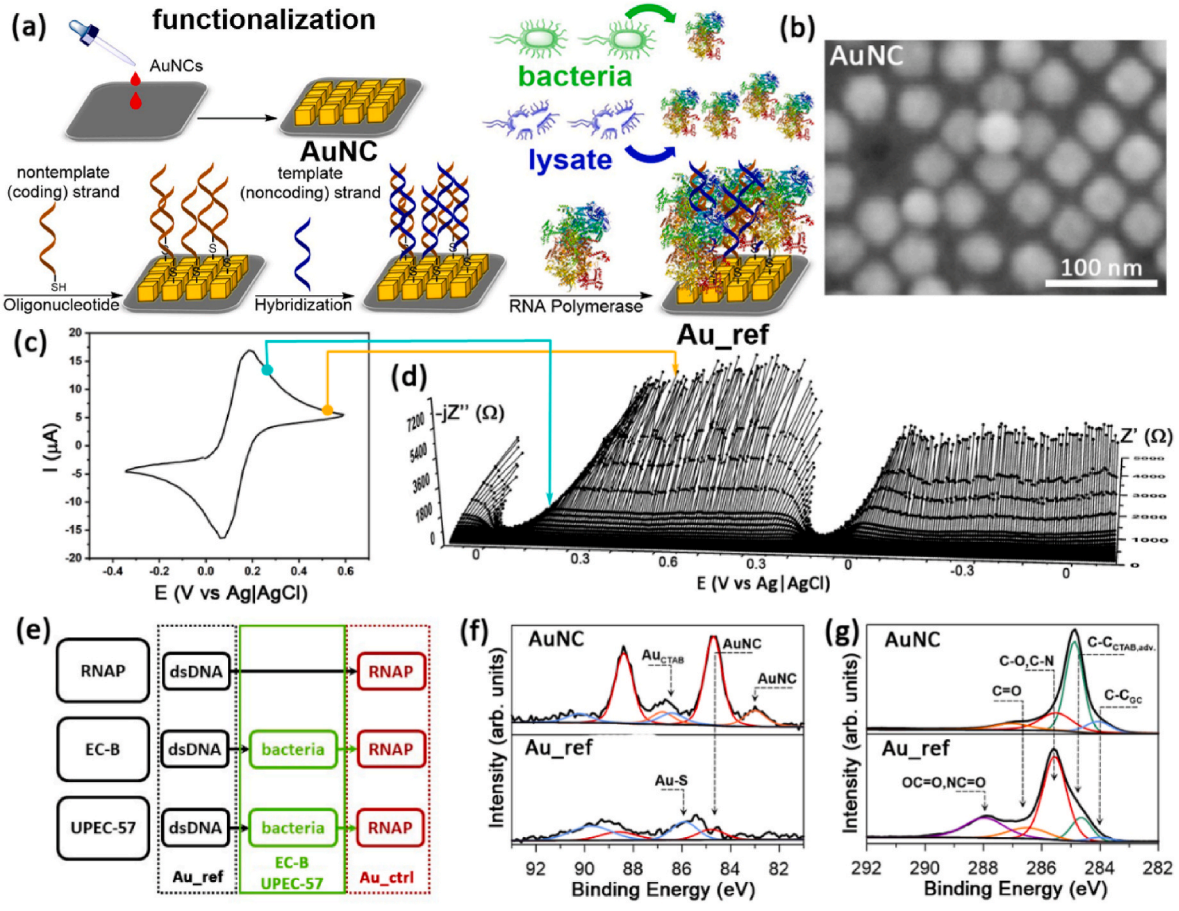

Fig. 1. (a) scheme of GCE decoration with AuNC and functionalization toward RNAP recognition; (b) SEM micrograph of drop-cast AuNC at GCE; (d) exemplary CV and (e) DEIS impedance plot obtained during the CV scan, with arrows identifying individual spectra collected at a given polarization; (e) identification of electroanalytical experiment labels; (f,g) high-resolution XPS spectra with proposed deconvolution for AuNCs at GC before and after functionalization with dsDNA: (f) *Au 4f* and (g) *C 1s*.

MOST WIEDZY Downloaded from mostwiedzy.pl

residue. A homogeneous GCE surface modified with AuNCs was obtained according to the previously described procedure (Niedzialkowski et al., 2022).

For the functionalization, as schematically presented in Fig. 1a, we used the sequence of one of the P1 promoters, $p_{rrnG\text{-}P1}$, allowing for the transcription of rRNA genes of the *rrnG* operon. The selected promoter sequence enabled the binding of *E. coli* RNAP and thus was effectively used as a biosensor receptor. AuNCs were modified by applying 200 μL of 0.2 μmol/L nontemplate (coding) oligonucleotide strand dissolved in TRIS-HCl buffer, pH 7.56. After a 12-h modification at room temperature, the electrode surface was thoroughly rinsed with Tris HCl buffer, pH 7.56. Then, a hybridization process was performed using an oligonucleotide with a complementary sequence. The 200 μL of 0.1 μmol/L template (noncoding) oligonucleotide stand dissolved in TRIS-HCl buffer, pH 7.56, was placed on the electrode surface and left for 2 h at room temperature. Such functionalized electrodes served for RNAP detection.

2.3. Biorecognition methodology

The Multiparametric Impedance Discriminant Analysis (MIDA) combines multisine impedimetric monitoring with singular value decomposition of raw impedance data, followed by partial least squares discriminant analysis. No electric equivalent circuit was used during impedance data analysis. All electrochemical measurements were performed in the three-electrode setup, with AuNC drop-cast and functionalized at GCE as the working electrode (0.38 cm^2 electrolyte-exposed area), silver chloride-coated silver wire (150 x 1.5 mm) as the reference electrode, and coiled platinum wire (100 x 0.5 mm) as the auxiliary electrode. The impedance monitoring was performed using an AC signal consisting of a package of 21 elementary sinusoids, ranging from 3 to 4500 Hz, superimposed on a DC voltammetry scan, from −0.35 V to 0.60 V, scan rate 2 mV/s. The exact procedure was previously described by the authors (Brodowski et al., 2022; Niedzialkowski et al., 2020). Exemplary impedance spectra recorded during a voltammetry scan are given in Fig. 1c and d. An Autolab (PGSTAT30) potentiostat/galvanostat by Metrohm, The Netherlands, was linked to a computer equipped with a 24 Bit, 204.8 kS/s, PCI-4461 card by National Instruments, USA, and used to generate the AC perturbation signal package.

In the analysis, each impedance dataset at a specific bias (among the 1890 applied biases), is given by the measured complex impedance, expressed as follows (eq. (1)):

$$\mathbf{Z}_{bias} = \mathbf{Z}'_{bias} + j\mathbf{Z}''_{bias} \quad (1)$$

where $\mathbf{Z}_{bias}$ is a total impedance, $\mathbf{Z}'_{bias}$ and $\mathbf{Z}''_{bias}$ are the real and imaginary parts of $\mathbf{Z}_{bias}$, respectively, and $j^2 = -1$. Thus, $\mathbf{Z}_{bias}$ is a complex number matrix with dimensions of 18 (number of independent tests) × 21 (number of elementary frequencies in a single measurement). The 18 tests include six replicates for each condition (EC-B and UPEC-57 strains) assisted by a reference Au_ref study and control Au_ctrl study in excess of RNAP. In this manner, 1850 matrices were prepared for each experiment (the first 30 and last 10 measurements were discarded). No data centering or scaling was applied to the datasets.

To treat a large amount of collected data, singular value decomposition (SVD) is applied to complex impedance datasets. Let $\mathbf{Z}_{bias}$ be the above-reported 18×21 matrix, which can be decomposed with SVD into 3 matrices (eq. (2)):

$$\mathbf{Z}_{bias} = \mathbf{U}\mathbf{\Sigma}\mathbf{V}^T \quad (2)$$

where $\mathbf{\Sigma}$ is a matrix with real, nonnegative entries, σ_i, on the diagonal and zeros off the diagonal, organized so that $\sigma_1 > \sigma_2 > \ldots > \sigma_r$; and $\mathbf{U}$ and $\mathbf{V}$ are unitary orthonormal matrices. Different experimental conditions (e.g. the presence/absence of the analyte) were arranged in a matrix with each column containing all the measurements at a given frequency. Thus, if the columns of $\mathbf{Z}_{bias}$ are analyte measurements at a frequency, then $\mathbf{U}$ distinguishes the analyte patterns, and $\mathbf{V}$ encodes the frequency patterns. Hence, the right singular vectors could be interpreted as an EIS spectrum, or a linear combination of any, so it would be possible to reconstruct the original EIS by linear combinations of the singular EIS. Then, two different paths are followed.

Path 1: PLS Discriminant Analysis (PLS-DA) is a discrimination method based on PLS regression. A dummy response variable, y, was added to the dataset, which is equal to +1 for positive samples, and −1 for the control group. Now, considering the linear system of equations $\mathbf{y} = \mathbf{Z}_{bias}\,\mathbf{x}$, the goal is to determine the weighting $\mathbf{x}$ that relates to the presence of the bacteria, restricted to the first two components. For this aim, a truncated SVD (to the first three singular values) was employed. This path can provide useful information about the frequencies most involved in the sensing mechanism (Pierpaoli et al., 2022).

Path 2: Linear regression is performed on both real and imaginary (treated as real) parts of $\mathbf{u_1}$ and $\mathbf{u_2}$, using the same response variable, $\mathbf{y}$.

Finally, in order to evaluate the ideal polarization potential intervals (PPI) to better discriminate between control and positive samples, the conventional metrics, such as accuracy, sensitivity and specificity, were calculated as follows (eqs (3)–(5)) (Van Stralen et al., 2009):

$$\text{accuracy} = (TP + TN)/(TP + TN + FP + FN) \quad (3)$$

$$\text{sensitivity} = TP/(TP + FN) \quad (4)$$

$$\text{specificity} = TN/(TN + FP) \quad (5)$$

where TP = true positive, TN = true negative, FP = false positive, and FN = false negative.

Two strains of bacteria labeled, EC-B and UPEC-57, were presented in the form of suspended intact bacterial cells or bacterial lysate solution and studied in artificial and real human urine at a volume ratio of 1:1 with 0.01 M PBS containing 1 mM $Fe(CN)_6^{3-/4-}$. Real human urine was obtained from a healthy 37-year-old woman, co-author of this publication. The analysis was carried out in a medical laboratory of Diagnostyka SA, Poland. The parameters of the urine tested are presented in the SI file, Table S1. The reference measurements (Au_ref) were carried out on the dsDNA functionalized electrode in the absence of the analyte. Each time, a control measurement (Au_ctrl) was also performed, admixing 1 CFU E. *coli* RNAP to the previously used solution, see Fig. 1e for experiment scheme. Prior to electrochemical measurements, the solution was heated to 37 °C using an Eppendorf ThermoMixer. By spiking the real human urine with 3 different concentrations of UPEC-57, and using above described, LOD was estimated using the median and standard deviation of the blank samples using the following equation (6):

$$LOD = CFU_{median} + 3 \times SD_{CFU} \quad (6)$$

2.4. Physicochemical analyses

X-ray photoelectron spectroscopy (XPS) analyses were carried out in the core-level binding energy range of *C 1s*, *Au 4f*, *O 1s* and *N 1s* to investigate the surface chemistry of the biosensor surface after consecutive functionalization steps, i.e. AuNC drop-casting at GCE and dsDNA grafting. These studies were carried out on an Escalab 250Xi (ThermoFisher Scientific), utilizing an AlKα X-ray source, spot diameter of 250 μm and pass energy of 20 eV. Low-energy electron and low-energy Ar^+ ion bombardment were used for charge compensation purposes. Avantage v5.9921(ThermoFisher Scientific) was used for deconvolution and peak calibration using adventitious carbon *C 1s* (284.6 eV).

Atomic force microscopy (AFM) studies were performed with NTgra Prima (NT-MDT) and using NSG30 probes with geometric parameters 125x40x4 μm, resonant frequency 320 kHz, and spring constant 40 N/m. A set of 25 approximation curves were made in a rectangular area (side – 3.5 μm) for statistical processing purposes. The static technique

MOST WIEDZY Downloaded from mostwiedzy.pl

was used. These measurements were conducted in the electrolyte used for the electrochemical studies, under a potentiostatic regime at three different polarization potentials, namely: −0.3 V, +0.1 V and +0.5 V vs Ag/AgCl, before and after RNAP exposure to dsDNA-functionalized AuNC at GCE. The scanning electron microscopy (SEM) analysis was performed using Quanta 250 FE-SEM (FEI), with the operating electron beam at a 20 kV accelerating voltage.

3. Results and discussion

3.1. dsDNA immobilization on gold nanocubes

The efficacy of consecutive electrode functionalization steps was verified directly by means of XPS analysis, and indirectly through impedimetric changes analysis. Fig. 1f and **g** reveal the high-resolution XPS spectra registered in the core-level binding energy range of the *Au 4f* and *C 1s* peaks, respectively. Following Fig. 1f, one can observe a strong *Au* $4f_{7/2}$ component at 84.7 eV, testifying the presence of AuNC at the GC surface. Two more peak doublets were identified, the one shifted at −1.5 eV is likely ascribed to an AuNC surface component

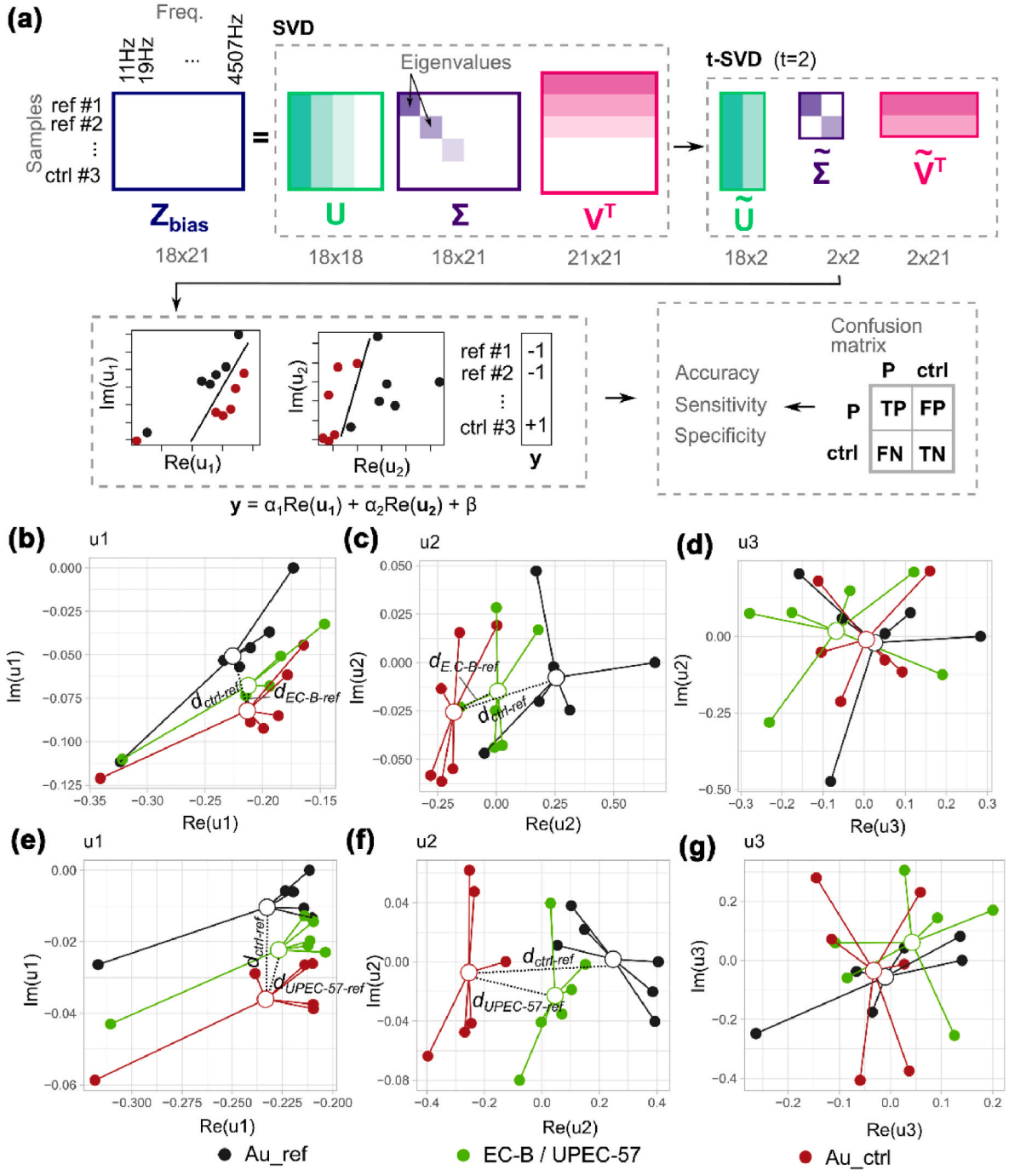

Fig. 2. (a) Schematic of the data elaboration, with an example for $N_p = 1760$ and $E_p = -0.28$ V; (b–g) Graphical representation of the first three columns of U: (b–d) for the EC-B, and (e–g) UPEC-57 datasets.

MOST WIEDZY Downloaded from mostwiedzy.pl

(Niedzialkowski et al., 2022; Passiu et al., 2020), while the one at +1.6 eV should be interpreted as Au-C moieties, thus testifying to Au complexing by surfactant, CTAB, as discussed in more detail in another report on AuNC chemistry (Niedzialkowski et al., 2022). Anchoring the thiol-functionalized oligonucleotide strand and hybridizing the complementary strand to obtain the dsDNA receptor led to an increase in the layer thickness, suppressing the Au signal. Notably, after surface functionalization, the primary constituent is the peak at 85.8 eV, which is characteristic of Au species involved in the Au-S bond (Laomeephol et al., 2020; Vitale et al., 2011). In the case of the GCE surface with drop-cast AuNCs, the major constituents of the *C 1s* spectra are the 284.8 and 285.6 eV peaks, attributed to aliphatic C-C and C-N/C-O bonds, respectively, from the presence of CTAB and adventitious carbons, with a smaller component from the sp^2-C within the GCE substrate (Dwivedi et al., 2015; Qu et al., 2019). Anchoring the dsDNA receptor significantly alters the surface chemistry of the sensor. The strongest signal originates from the C-O/C-N bonds and OC═O, NC═O bonds, present within the hydrocarbon chains in nucleic acid bases. This observation is typical of DNA anchored at electrode surfaces (Niedzialkowski et al., 2020; Silva-Moraes et al., 2018). A significant drop in the share of sp^2-C corroborates the increase in the functionalization layer.

Consecutive steps of surface functionalization, depicted in Fig. 1a, were routinely controlled by electrochemical impedance spectroscopy and cyclic voltammetry; see the data in the SI file, Fig. S1 and Table S2. As a general rule, the next functionalization steps lead to an increase in the thickness of the layer functionalized at the electrode surface, which successively increases the charge transfer resistance, R_{CT}.

3.2. Data analysis and RNA polymerase recognition in real bacteria cultures

The impedimetric data treatment is schematically reported in Fig. 2a. The first step in analyzing the data was to perform SVD for each polarization step. In the first part of the experiment, the recognition of real bacteria cultures was carried out in artificial urine. As an example, the real against the imaginary part of the first three columns of **U** are reported, for both the EC-B and UPEC-57 datasets, at $N_p = 1760$ ($E_p = -0.28$ V) in Fig. 2b–g, showing that the greatest separation between control and positive samples is given both by the real and imaginary part of the first component and by the real part of the second component. No distinction is provided by the third component (as also reported by the low explained variance). For this reason, the PLS-DA was conducted with truncated SVD (t-SVD), with r = 2. Moreover, the Euclidean distances $d_{ctrl\text{-}ref}$, $d_{E.coli\text{-}ref}$ and $d_{UPEC\text{-}ref}$ have been defined as the distance between the centroids. A similar observation can be made regardless of whether the analysis is done on suspended bacteria or bacterial lysate (see SI file, Fig. S2 for details). Since the first column, $\mathbf{u_1}$, carries most of the dataset information, it is possible to see that the individual points are characterized by high dispersion, which may be related to the characteristics of the single electrode, which results from the fabrication steps. On the other hand, in $\mathbf{u_2}$, the different tests are well-clustered, suggesting that this component may be connected to the bacteria identification, independently of the different electrode characteristics. Indeed, minor features that distinguish the different impedance measurements are common and will most likely be represented by components different from the first. This behavior can be observed for both the EC-B and UPEC-57 datasets.

By performing the SVD analysis reported above at all the 1850 polarization steps (N_p), it was possible to observe how the sample clustering varies with the application of a polarization potential (E_p). The variation of the specificity, accuracy, and sensitivity as a function of N_p is shown in Fig. 3a for EC-B and Fig. 3b for UPEC-57. It is possible to see, for EC-B, the more pronounced presence of some intervals in which a dramatic drop in the sensitivity is present, which corresponds with the second component, showing a slight increase of the explained variance (Fig. 3c and d). By computing the previously defined Euclidean distances between centroids, it is possible to see distances maximization occurring at negative potentials (Fig. 3e and f). Similarly, to highlight the polarization potential intervals (PPIs) at which the distinction between sample sensitivity, accuracy, and specificity is most noticeable were calculated as functions of E_p (Fig. 3g,i). In particular, it is possible to observe the presence of three different behaviors at different electrode polarization

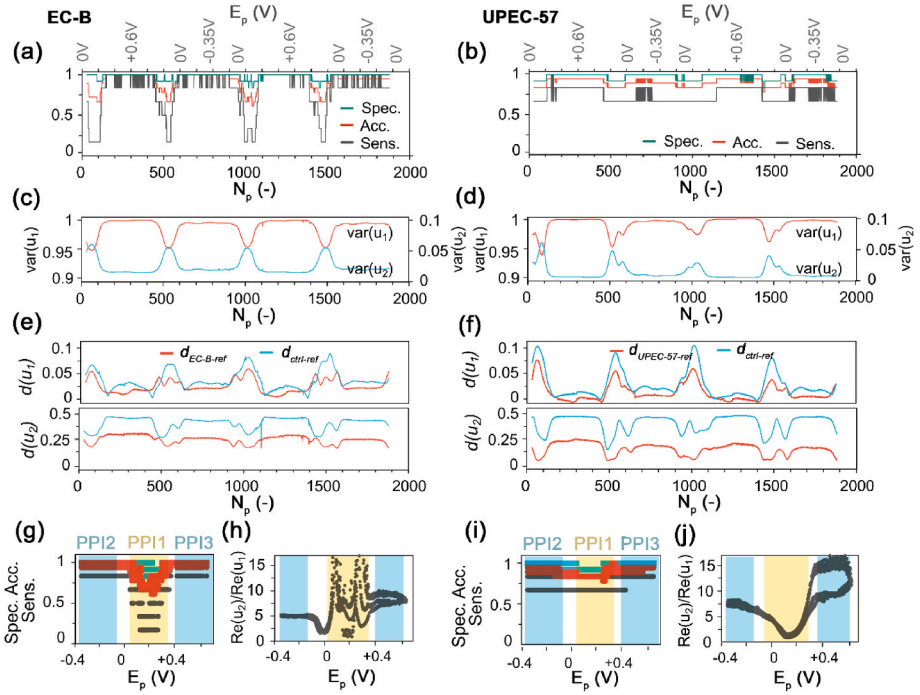

Fig. 3. Plot of specificity, accuracy and sensitivity as a function of N_p, for both (a) EC-B and (b) UPEC-57 datasets. Total variance explained by the first two columns of **U** for (c) EC-B and (d) UPEC-57. (e,f) Euclidean distance between the centroids given by the different test conditions, for $\mathbf{u_1}$ and $\mathbf{u_2}$. (g,i) plot of the specificity, accuracy and sensitivity as a function of E_p. (h,j) ratio between the real part of $\mathbf{u_1}$ and $\mathbf{u_2}$.

MOST WIEDZY Downloaded from mostwiedzy.pl

conditions:

1) **PPI1** (-0.1 V $< E_p <$ $+0.3$ V). Interval in which the oxidation (or reduction) of the redox probe is not suitable for analyte detection.
2) **PPI2** ($E_p < -0.1$ V): Optimal interval for the bacteria detection, excluding the measurement performed close to the inversion potential. The Euclidean distance between the samples' (reference vs. control) centroids is slightly higher, suggesting better discrimination.
3) **PPI3** ($E_p > +0.4$ V): Suitable interval for the bacteria detection.

A conclusion may be drawn from the above analysis, suggesting that polarization with low overpotentials should be avoided due to its vicinity to the redox potential of the $[Fe(CN)]_6^{3-/4-}$ probe used in this study. The redox potentials may be subject to slight changes in-between particular experiments due to inevitable differences in the electric properties and, as an effect, the reversibility of the redox process at receptor-functionalized surfaces. This effect will exacerbate the accuracy and sensitivity drop of the biosensor when comparing results from many experiments. Identification of the decreased accuracy and sensitivity of the impedimetric analyses in **PPI1** is of paramount importance, since not only the redox potentials but also the formal potential E_F lies in the above interval. E_F is estimated based on anodic (E_a) and cathodic (E_c) voltammogram peaks, $E_F = (E_a - E_c)/2$ and is defined as the reduction potential applying to a half-reaction under a specific set of conditions, therefore it is typically considered to be electrode polarization conditions in the vast majority of impedimetric biosensor studies. The in-depth SVD analysis shown here suggests that the accuracy and sensitivity of EIS biosensors may be suboptimal at low overpotentials (**PPI1** polarization range). On the other hand, the necessity to meet the stationary condition in classic EIS studies makes it impossible to perform studies at higher anodic or cathodic overpotentials.

The cathodic (**PPI2**) or anodic (**PPI3**) overpotentials must be applied to efficiently distinguish between the control and positive samples. The detection may be related to diffusion-surface kinetic processes, since the contributions of frequencies in the low range are predominant (see SI file, Fig. S3, in particular the interval FI1 for frequencies below 20Hz), where studies by Settu et al. (2015) suggest a maximum relative changes measured at 10 Hz. At negative polarization potential, the same $Re(u_2)/Re(u_1)$ ratio for both anodic and cathodic scan may suggests the existence of the same electrochemical behaviour, while, at positive polarization, the presence of an hysteresis loop may be indicator of two different behaviours for anodic and cathodic scans, as reported in Fig. 3h,j.

In light of the above considerations, Fig. 3e and f shows the distance between centroids for the first two columns of U, that the samples with real bacterial cultures find a place between the control and the reference. By using the same coefficients determined for the PLS-DA, the detection of UPEC-57 in artificial urine was performed, resulting in an averaged sensitivity, accuracy and specificity of 80, 90, 93% respectively, for the negative polarization interval (Fig. 3i). In general, the effect of electrode polarization potential on differentiating between the absence and presence of bacteria is more pronounced for EC-B than for UPEC-57. In particular, this is strongly penalized within the range bounded by the reduction and oxidation potentials of the redox probe; however, UPEC-57 is less affected (Fig. 3b). In conclusion, no significant differences in signal response were observed between EC-B and UPEC-57, which means that the proposed biosensor is not specific towards a given *E. coli* bacteria strain. Importantly, in the light of current diagnostic recommendations (Hay et al., 2016; Nicolle et al., 2019), the specificity of the method used to detect bacteria in the urine is not crucial. According to the medical dogma (Kass, 1962), the human urine of a healthy person should be sterile and UTI is typically thought to be caused by the presence of bacteria in the urine of a symptomatic patient.

3.3. UPEC-57 detection in real human urine

Detection in real media, such as human urine, is significantly more difficult compared to synthetic electrolytes, as it is characterized by chemical and biological diversity, containing up to 3000 different organic compounds and metabolites, including proteins, carbohydrates, and blood cells (Sarigul et al., 2019). To verify the utility of the developed methodology in the human urine environment, a procedure analogous to that described in the previous section was carried out. As expected, the studies in a real environment, with an unknown concentration of fouling agents, such as proteins and metabolites (Hanssen et al., 2016) led to a decrease in the averaged sensitivity, accuracy and specificity, now on the level of 83, 80 and 83%, respectively (averaged values at negative polarization potential) (Fig. 4a). When PLS regression was performed using t-SVD in real urine, **PPI2** was found to be superior to **PPI3** for UPEC-57 detection, see Fig. 4c and d, in the first polarization cycle, and that the sensing ability worsened with the increasing N_p. Indeed, after the first scan, it is possible to appreciate a loss in R^2, probably due to some irreversible processes taking place on the electrode surface (Fig. 4b).

The estimated LOD of UPEC-57 in human urine reaches 11.3 CFU/mL when studied at negative overpotentials of **PPI2** range. This result matches or surpasses most other available reports, while obtained using simple electrode surface architecture. A comparative study of different *E. coli* sensors in human urine is presented in Table 1, while electrochemical biosensors in other electrolytes are also given in the SI file, Table S3. Moreover, we have confirmed that the LOD of the method proposed here is 10x lower compared to the commonly used bacteria cultivation technique in which the detection of bacterial colonies is performed by plating of the bacterial solution onto Petri dishes with solid LA medium and overnight incubation. With this culture protocol, we were able to detect UPEC-57 bacteria in a solution that contained at least 10^2 bacterial cells per 1 mL (CFU/mL). The illustrative plates with bacterial colonies obtained by using the cultivation-based detection method are shown in Fig. 4f. For comparison, the proposed approach shows a limit of detection of 11.3 CFU/mL for the uropathogenic *E. coli* strain No. 57. Indeed, a similar LOD can be reached by using an enrichment procedure followed by molecular detection, however, this approach will take much more time (around 24 h) than the proposed by us method. On the other hand, our impedimetric analysis takes as little as 2 min, which results from polarization in the **PPI2** range (-0.35 to -0.10 V, with 2 mV/s), while no conditioning in real media was necessary.

It should be noted that, unlike in the artificial electrolyte, carrying out the analysis of several studied samples under deep anodic polarization have led to irreversible changes occurring at the biosensor surface. This process is associated with the accumulation of compounds present in urine (i.e. carbohydrates, proteins, and leukocytes) at the electrode surface, passivating it and blocking the electrode. In approx. 60% of these events, the surface passivation led to biosensor damage, as shown in Fig. 4e and SI file, Fig. S4. The voltammograms presented in the SI file, Fig. S5, reveal additional redox processes associated with the oxidation of uric acid. It should be noted that such behavior did not occur when the biosensor was subjected only to cathodic polarization in the **PPI2** range. Even when the passivation is incomplete, the above-described behavior explains the significantly lower biosensor accuracy when studied in the anodic polarization range, as shown in Fig. 4b, c and 4e.

The DEIS and PLS-DA approach provides valuable information about measurement conditions that could lead to electrode degradation, enabling users to take preventive measures. The analytical limits of any sensor can be adjusted to the individual needs by varying the applied polarization (in this case, **PPI2**) or frequency range. The utilization of adjusted frequency has been demonstrated to enhance sensor performance and improve the efficiency of machine learning algorithms, as previously observed (Kokabi et al., 2023; Xu and Hong, 2022). The

MOST WIEDZY Downloaded from mostwiedzy.pl

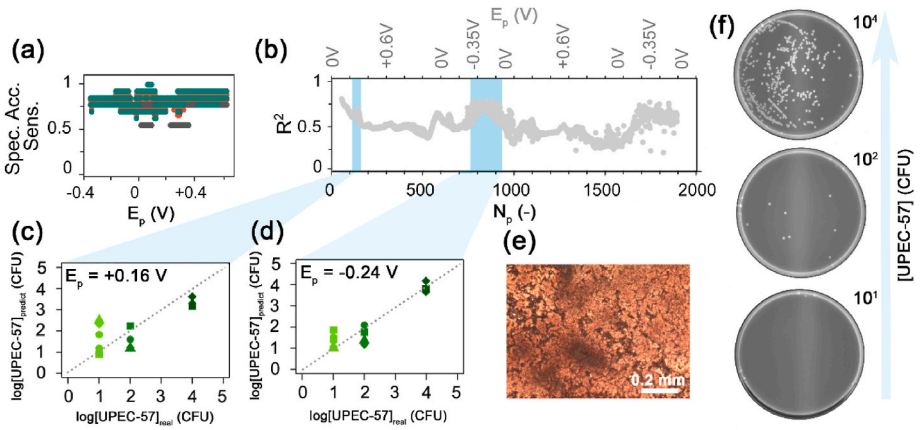

Fig. 4. Plot of (a) the specificity, accuracy and sensitivity and (b) R^2 as a function of E_p for UPEC-57 in real urine; difference between real and predicted values of UPEC-57 concentrations at (c) positive and (d) negative polarization potential; (e) optical microscope image of damaged surface; (f) illustrative plates with bacterial colonies obtained by using the cultivation-based detection method.

Table 1
E. coli LOD and detection time in real urine using different detection methods.

Detection method	Type of substrate	Detection time	LOD (CFU/mL)	Ref.
Spectrofluorometry	Receptor-binding proteins on MNPs	1.5 h	~10^7	Costa et al. (2022)
PCR	Marker genes	1 h	10^4	Brons et al. (2020)
Bacteria cultivation	Bacterial colony number per 1 mL suspension	16–20 h	~10^2	This work
Electroporation	Segregation of nonreplicating plasmid pGTR902	22 min	10^2	Forsyth et al. (2018)
Microfluidic capillaric circuit	Antibody-functionalized microbeads	<7 min	120	Olanrewaju et al. (2017)
Fluorescence	Bacterial nuclease activity	1 h	<500	Flenker et al. (2017)
Fluorescence	Mannose-modified polyethyleneimine copolymer particles	~1 h[a]	265	Li et al. (2019)
CV-DPV	Au@MoS_2–PANI on GCE	30 min	10	Raj et al. (2021)
CV	PANI/AuNP composite on SPCE	~60 min[a]	4	Shoaie et al. (2018)
EIS	Interdigitated Au microelectrode	1–12 h	7	Settu et al. (2015)
LSV	Unspecified carbon electrode	35 min	24	Safavieh et al. (2012)
CV-DPV	rGO/polyethyleneimine-modified Au	~35 min[a]	10	Jijie et al. (2018)
CV	Thionine dye (Th) on MWCNT/chitosan coated on GCE	1 h	50	Gayathri et al. (2016)
MIDA	AuNC drop-cast on GCE	~2 min	11.3	This work

[a] information not available directly, the detection time is speculated based on the experimental steps provided.

utilization of Arduino microcontrollers enables the implementation of a multi-frequency approach, offering a user-friendly monitoring tool for therapy that can be easily operated by inexperienced individuals. (Merli et al., 2020; Murillo-Ortiz et al., 2020; Romero Coripuna et al., 2021; Wang, 2015).

A detailed understanding of the altered biosensor response depending on the applied overpotential is extremely difficult due to the complexity of the electrode surface, both in terms of the macromolecular structure and resultant, instantaneous surface charge distribution. To shed light on the role played by the charged-up electrode surface, we calculated the electrostatic potential based on the Poisson-Boltzmann equation for the macromolecules functionalized at the AuNC surface and conducted spectroscopic AFM studies of the proposed biosensors. Notably, neither the AuNC surface charge nor the solvent could be considered in these calculations. Fig. 5a shows a model of dsDNA attached covalently to AuNC and the RNAP. Since DNA bears a highly negative formal charge, due to the presence of negatively charged phosphate moieties linking neutral nucleosides, one can assume that upon oligonucleotide immobilization, the surface of the functionalized gold cubes becomes highly negative and remains negative upon DNA hybridization. On the other hand, RNAP is a complex system with some domains bearing a total negative and some positive charge, although most of the RNAP subunits have more negatively charged amino acids (D/E) than positively charged (K/R), resulting in a theoretical value of isoelectric points in the range of 4.5–5.2. In particular, the RNAP domain responsible for DNA binding is highly positive, so upon DNA binding, the DNA–protein complex is stabilized not only via specific van der Waals interactions and hydrogen bonds but also electrostatic interactions. Upon binding, the entire complex has an excess of negative charge and most of the protein domains binding DNA also become negatively charged due to the presence of dsDNA (Fig. 5b). However, our modeling predicts some RNAP domains (composed mostly of subunit alpha) that are positioned close to the gold surface, and that bear only a slightly negative electrostatic charge. As a result, upon RNAP binding, the electrostatic charge in the vicinity of the gold surface changes from highly negative to less negative/neutral, which is likely detected in the experimental setup.

The spectroscopic AFM mode is based on force imaging of the probe positioned on the sample surface, registering the change in the selected physical quantity. In this particular case, we registered the approach curves of the AFM probe to the functionalized electrode surface at electrode potentials falling in the **PPI1**, **PPI2** and **PPI3** range. The approach makes it possible to register the mechanical characteristics of dependence between the interaction force as a function of the probe–sample separation (Cappella and Dietler, 1999), where the process of transition between the non-contact and the contact mode of interaction can manifest via different shapes of the approach curves (Wu, 2010). In the first stage, the AFM probe approaches the surface, and when the attractive forces prevail over the spring constant of the lever, the probe jumps to a set-up position in the vicinity of the tested surface, marking the probe–sample distance, as illustrated in Fig. 5c. The AFM probe elongation, h, is inversely proportional to the thickness of the functionalized film. It should be noted, however, that neither the current

MOST WIEDZY Downloaded from mostwiedzy.pl

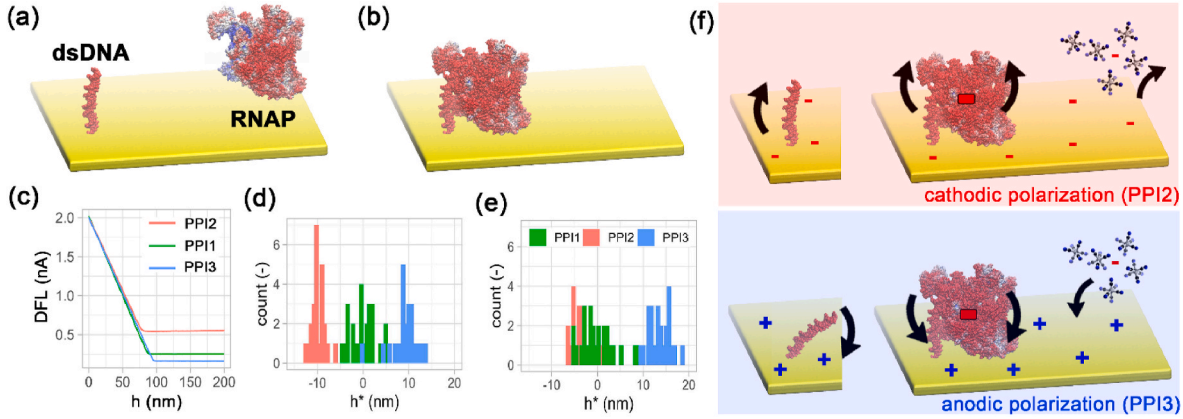

Fig. 5. (a) calculated electrostatic potential for DNA model on AuNC and RNAP sigma70 complex; and (b) RNAP-DNA complex model on AuNC. Red color corresponds to the negative electrostatic charge and blue color corresponds to the positive electrostatic charge; the more intensive the color, the stronger the negative/positive charge. (c) Exemplary AFM approach curve for the dsDNA functionalized Au_ref sample; piezoelectric elongation of: (d) Au_ref and (e) Au_ctrl at various electrode polarizations. (f,g) Scheme of coulombic forces between the functionalization film and the AuNC substrate, affecting charge transfer process at differently polarized electrode surface.

deflection of the AFM probe nor the current height of the sample at the contact point is known *a priori*, thus the approach curves provide only an indirect measure of changes in the conformation of the studied system depending on the applied polarization potential. Therefore, the probe–sample distance was normalized, setting the sample studied in the **PPI1** range as the reference (h* = 0). The h* value should be considered in terms of changes in the strength of interatomic interactions between the macromolecules and the atoms of the microscope tip. Fig. 5d shows the results of a statistical analysis from 25 approach curves to the Au_ref electrode surface. When these data are taken only in the context of changes in the conformation of the macromolecular film at the electrode surface, it can be concluded that polarization in the anodic **PPI2** range reduces the film thickness (compared to **PPI1**), while polarization in the cathodic direction (**PPI3**) causes the opposite effect. Similar changes in the orientation of dsDNA in the electric field were reported previously (Meunier et al., 2015; Niedzialkowski et al., 2020). The final effect on the macromolecule's conformation is visible upon RNAP interaction with the dsDNA at the electrode surface, as in Au_ctrl (Fig. 5e). The presence of coulombic repulsion between a negatively charged RNAP-DNA complex and the negatively charged electrode surface (**PPI2**) produces a similar effect to the one discussed above, but the h* decrease is much smaller, possibly due to the steric hindrance effects by the RNAP-DNA complex.

The processes discussed may have a multidimensional influence on the measured impedimetric parameters. The most commonly used indicator, R_{CT}, will notably increase upon RNAP-DNA interaction, developing the functionalized layer thickness, and hindering the diffusion of the negatively charged ferrocyanide redox probe. It should also be noted that the higher the functionalized layer thickness, the smaller the measured capacitance. The change in electrode conformation has an immediate effect on the frequency dispersion of the capacitance, as previously discussed (Niedzialkowski et al., 2020). The effect of electrode polarization under **PPI2** and **PPI3** conditions is schematically illustrated in Fig. 5f, suggesting a possible mechanism of molecular interactions in the electric field that allows one to distinguish the impedimetric signal in the presence and in the absence of the RNAP. Due to the complexity of the studied interphase, however, any experimental or simulation technique will provide an impaired and incomplete interpretation of the studied process. Nevertheless, the combined DEIS with PLS-DA approach makes it possible to effectively identify the unique impedimetric fingerprint of the biosensor studied.

4. Conclusions

We proposed a new methodology for biosensor operation, which utilizes real-time impedimetric monitoring combined with partial least squares discriminant analysis. The principle of its operation is to distinguish the presence of the analyte not only by strong intermolecular forces but also by weak coulombic forces, when measured under different polarization conditions, to obtain the explicit impedimetric fingerprint of the macromolecular interactions.

As a proof-of-concept of the methodology, we selected the aptameric recognition of RNAP for two different *E. coli* strains, including uropathogenic UPEC-57. The approach discriminates the presence of the analyte at very low concentrations directly in the real human urine environment, despite the presence of an unknown amount and concentration of fouling agents. The impedimetric analysis was carried out on raw data, without fitting with electric equivalent circuits. The study revealed that the detection is most accurate at negative overpotentials (−0.35 to −0.10 V vs Ag/AgCl), where the interaction between negatively charged $[Fe(CN)]_6^{3-/4-}$ species and negatively charged RNAP-DNA complexes at AuNC should result in the increase of charge transfer resistance and introduce frequency dispersion of capacitance effects. Our study shows the capability of UPEC-57 identification with a LOD reaching 11.3 CFU/mL after only 2 min and using a simple glassy carbon electrode architecture with drop-cast, self-organizing Au nanocube patterns. Although there are differences between the data collected for EC-B and UPEC-57, the biosensor is not capable of distinguishing between two strains of *E. coli*.

CRediT authorship contribution statement

Adrian Koterwa: Validation, Formal analysis, Investigation, Data curation. **Mattia Pierpaoli:** Methodology, Software, Validation, Formal analysis, Investigation, Data curation, Writing – original draft, Visualization. **Bożena Nejman-Faleńczyk:** Methodology, Writing – original draft, Writing – review & editing. **Sylwia Bloch:** Validation, Investigation, Writing – original draft. **Artur Zieliński:** Investigation, Writing – original draft. **Wioletta Adamus-Białek:** Resources, Writing – review & editing. **Zofia Jeleniewska:** Investigation, Writing – original draft. **Bartosz Trzaskowski:** Formal analysis, Writing – original draft, Writing – review & editing, Visualization. **Robert Bogdanowicz:** Conceptualization, Writing – original draft, Writing – review & editing. **Grzegorz Węgrzyn:** Resources, Writing – review & editing. **Paweł Niedziałkowski:** Methodology, Investigation, Resources, Writing – original draft, Writing – review & editing, Supervision. **Jacek Ryl:** Conceptualization,

MOST WIEDZY Downloaded from mostwiedzy.pl

Methodology, Investigation, Writing – original draft, Writing – review & editing, Visualization, Supervision, Funding acquisition.

Declaration of competing interest

The authors declare that they have no known competing financial interests or personal relationships that could have appeared to influence the work reported in this paper.

Data availability

Data will be made available on request.

Acknowledgments

This work was supported by the National Science Centre (Republic of Poland) under project 2020/37/B/ST7/03262. Financial support of these studies from Gdańsk University of Technology under the Nobelium – "Excellence Initiative – Research University" program (M. Pierpaoli) is gratefully acknowledged.

Appendix A. Supplementary data

Supplementary data to this article can be found online at https://doi.org/10.1016/j.bios.2023.115561.

References

Abedi, R., Bakhsh Raoof, J., Bagheri Hashkavayi, A., Asghary, M., 2021. Highly sensitive and label-free electrochemical biosensor based on gold nanostructures for studying the interaction of prostate cancer gene sequence with epirubicin anti-cancer drug. Microchem. J. 170, 106668 https://doi.org/10.1016/j.microc.2021.106668.

Aitekenov, S., Gaipov, A., Bukasov, R., 2021. Review: detection and quantification of proteins in human urine. Talanta 223, 121718. https://doi.org/10.1016/j.talanta.2020.121718.

Ali, M.R., Bacchu, M.S., Setu, M.A.A., Akter, S., Hasan, M.N., Chowdhury, F.T., Rahman, M.M., Ahommed, M.S., Khan, M.Z.H., 2021. Development of an advanced DNA biosensor for pathogenic Vibrio cholerae detection in real sample. Biosens. Bioelectron. 188, 113338 https://doi.org/10.1016/j.bios.2021.113338.

Bae, B., Feklistov, A., Lass-Napiorkowska, A., Landick, R., Darst, S.A., 2015. Structure of a bacterial RNA polymerase holoenzyme open promoter complex. Elife 4, e08504. https://doi.org/10.7554/eLife.08504.

Bhattacharjee, G., Majumder, S., Senapati, D., Banerjee, S., Satpati, B., 2020. Core-shell gold @silver hollow nanocubes for higher SERS enhancement and non-enzymatic biosensor. Mater. Chem. Phys. 239, 122113 https://doi.org/10.1016/j.matchemphys.2019.122113.

Brodowski, M., Pierpaoli, M., Janik, M., Kowalski, M., Ficek, M., Slepski, P., Trzaskowski, B., Swain, G., Ryl, J., Bogdanowicz, R., 2022. Enhanced susceptibility of SARS-CoV-2 spike RBD protein assay targeted by cellular receptors ACE2 and CD147: multivariate data analysis of multisine impedimetric response. Sensor. Actuator. B Chem. 370, 132427 https://doi.org/10.1016/j.snb.2022.132427.

Brons, J.K., Vink, S.N., de Vos, M.G.J., Reuter, S., Dobrindt, U., van Elsas, J.D., 2020. Fast identification of Escherichia coli in urinary tract infections using a virulence gene based PCR approach in a novel thermal cycler. J. Microbiol. Methods 169, 105799. https://doi.org/10.1016/j.mimet.2019.105799.

Cappella, B., Dietler, G., 1999. Force-distance curves by atomic force microscopy. Surf. Sci. Rep. 34, 1–104. https://doi.org/10.1016/S0167-5729(99)00003-5.

Chapman, C.A.R., Chen, H., Stamou, M., Biener, J., Biener, M.M., Lein, P.J., Seker, E., 2015. Nanoporous gold as a neural interface coating: effects of topography, surface chemistry, and feature size. ACS Appl. Mater. Interfaces 7, 7093–7100. https://doi.org/10.1021/acsami.5b00410.

Chen, F., Tang, Q., Ma, T., Zhu, B., Wang, L., He, C., Luo, X., Cao, S., Ma, L., Cheng, C., 2022. Structures, properties, and challenges of emerging 2D materials in bioelectronics and biosensors. InfoMat 4. https://doi.org/10.1002/inf2.12299.

Cimafonte, M., Fulgione, A., Gaglione, R., Papaianni, M., Capparelli, R., Arciello, A., Bolletti Censi, S., Borriello, G., Velotta, R., Della Ventura, B., 2020. Screen printed based impedimetric immunosensor for rapid detection of Escherichia coli in drinking water. Sensors 20, 274. https://doi.org/10.3390/s20010274.

Clock, S.A., Planet, P.J., Perez, B.A., Figurski, D.H., 2008. Outer membrane components of the tad (tight adherence) secreton of *Aggregatibacter actinomycetemcomitans*. J. Bacteriol. 190, 980–990. https://doi.org/10.1128/JB.01347-07.

Costa, S.P., Cunha, A.P., Freitas, P.P., Carvalho, C.M., 2022. A phage receptor-binding protein as a promising tool for the detection of Escherichia coli in human specimens. Front. Microbiol. 13, 871855 https://doi.org/10.3389/fmicb.2022.871855.

Davenport, M., Mach, K.E., Shortliffe, L.M.D., Banaei, N., Wang, T.-H., Liao, J.C., 2017. New and developing diagnostic technologies for urinary tract infections. Nat. Rev. Urol. 14, 296–310. https://doi.org/10.1038/nrurol.2017.20.

Deshmukh, R., Prusty, A.K., Roy, U., Bhand, S., 2020. A capacitive DNA sensor for sensitive detection of *Escherichia coli* O157:H7 in potable water based on the *z3276* genetic marker: fabrication and analytical performance. Analyst 145, 2267–2278. https://doi.org/10.1039/C9AN02291K.

Dwivedi, N., Yeo, R.J., Satyanarayana, N., Kundu, S., Tripathy, S., Bhatia, C.S., 2015. Understanding the role of nitrogen in plasma-assisted surface modification of magnetic recording media with and without ultrathin carbon overcoats. Sci. Rep. 5, 7772. https://doi.org/10.1038/srep07772.

Emilsson, G., Schoch, R.L., Feuz, L., Höök, F., Lim, R.Y.H., Dahlin, A.B., 2015. Strongly stretched protein resistant poly(ethylene glycol) brushes prepared by grafting-to. ACS Appl. Mater. Interfaces 7, 7505–7515. https://doi.org/10.1021/acsami.5b01590.

Felix, F.S., Angnes, L., 2018. Electrochemical immunosensors – a powerful tool for analytical applications. Biosens. Bioelectron. 102, 470–478. https://doi.org/10.1016/j.bios.2017.11.029.

Flenker, K.S., Burghardt, E.L., Dutta, N., Burns, W.J., Grover, J.M., Kenkel, E.J., Weaver, T.M., Mills, J., Kim, H., Huang, L., Owczarzy, R., Musselman, C.A., Behlke, M.A., Ford, B., McNamara, J.O., 2017. Rapid detection of urinary tract infections via bacterial nuclease activity. Mol. Ther. 25, 1353–1362. https://doi.org/10.1016/j.ymthe.2017.03.015.

Flores-Mireles, A.L., Walker, J.N., Caparon, M., Hultgren, S.J., 2015. Urinary tract infections: epidemiology, mechanisms of infection and treatment options. Nat. Rev. Microbiol. 13, 269–284. https://doi.org/10.1038/nrmicro3432.

Forsyth, V.S., Armbruster, C.E., Smith, S.N., Pirani, A., Springman, A.C., Walters, M.S., Nielubowicz, G.R., Himpsl, S.D., Snitkin, E.S., Mobley, H.L.T., 2018. Rapid growth of uropathogenic *Escherichia coli* during human urinary tract infection. mBio 9, e00186. https://doi.org/10.1128/mBio.00186-18. -18.

Frimodt-Møller, N., 2019. The urine microbiome – contamination or a novel paradigm? EBioMedicine 44, 20–21. https://doi.org/10.1016/j.ebiom.2019.05.016.

Gayathri, C.H., Mayuri, P., Sankaran, K., Kumar, A.S., 2016. An electrochemical immunosensor for efficient detection of uropathogenic E. coli based on thionine dye immobilized chitosan/functionalized-MWCNT modified electrode. Biosens. Bioelectron. 82, 71–77. https://doi.org/10.1016/j.bios.2016.03.062.

Glyde, R., Ye, F., Darbari, V.C., Zhang, N., Buck, M., Zhang, X., 2017. Structures of RNA polymerase closed and intermediate complexes reveal mechanisms of DNA opening and transcription initiation. Mol. Cell 67, 106–116.e4. https://doi.org/10.1016/j.molcel.2017.05.010.

Grine, G., Lotte, R., Chirio, D., Chevalier, A., Raoult, D., Drancourt, M., Ruimy, R., 2019. Co-culture of Methanobrevibacter smithii with enterobacteria during urinary infection. EBioMedicine 43, 333–337. https://doi.org/10.1016/j.ebiom.2019.04.037.

Gui, A.L., Luais, E., Peterson, J.R., Gooding, J.J., 2013. Zwitterionic phenyl layers: finally, stable, anti-biofouling coatings that do not passivate electrodes. ACS Appl. Mater. Interfaces 5, 4827–4835. https://doi.org/10.1021/am400519m.

Güner, A., Çevik, E., Şenel, M., Alpsoy, L., 2017. An electrochemical immunosensor for sensitive detection of Escherichia coli O157:H7 by using chitosan, MWCNT, polypyrrole with gold nanoparticles hybrid sensing platform. Food Chem. 229, 358–365. https://doi.org/10.1016/j.foodchem.2017.02.083.

Hanssen, B.L., Siraj, S., Wong, D.K.Y., 2016. Recent strategies to minimise fouling in electrochemical detection systems. Rev. Anal. Chem. 35, 1–28. https://doi.org/10.1515/revac-2015-0008.

Hay, A.D., Birnie, K., Busby, J., Delaney, B., Downing, H., Dudley, J., Durbaba, S., Fletcher, M., Harman, K., Hollingworth, W., Hood, K., Howe, R., Lawton, M., Lisles, C., Little, P., MacGowan, A., O'Brien, K., Pickles, T., Rumsby, K., Sterne, J.A., Thomas-Jones, E., Van Der Voort, J., Waldron, C.-A., Whiting, P., Wootton, M., Butler, C.C., on behalf of the DUTY team, 2016. The Diagnosis of Urinary Tract infection in Young children (DUTY): a diagnostic prospective observational study to derive and validate a clinical algorithm for the diagnosis of urinary tract infection in children presenting to primary care with an acute illness. Health Technol. Assess. 20, 1–294. https://doi.org/10.3310/hta20510.

Jijie, R., Kahlouche, K., Barras, A., Yamakawa, N., Bouckaert, J., Gharbi, T., Szunerits, S., Boukherroub, R., 2018. Reduced graphene oxide/polyethylenimine based immunosensor for the selective and sensitive electrochemical detection of uropathogenic Escherichia coli. Sensor. Actuator. B Chem. 260, 255–263. https://doi.org/10.1016/j.snb.2017.12.169.

Kass, E.H., 1962. Pyelonephritis and bacteriuria: a major problem in preventive medicine. Ann. Intern. Med. 56, 46. https://doi.org/10.7326/0003-4819-56-1-46.

Klein, R.D., Hultgren, S.J., 2020. Urinary tract infections: microbial pathogenesis, host–pathogen interactions and new treatment strategies. Nat. Rev. Microbiol. 18, 211–226. https://doi.org/10.1038/s41579-020-0324-0.

Kokabi, M., Sui, J., Gandotra, N., Pournadali Khamseh, A., Scharfe, C., Javanmard, M., 2023. Nucleic acid quantification by multi-frequency impedance cytometry and machine learning. Biosensors 13, 316. https://doi.org/10.3390/bios13030316.

Laomeephol, C., Ferreira, H., Yodmuang, S., Reis, R.L., Damrongsakkul, S., Neves, N.M., 2020. Exploring the gelation mechanisms and cytocompatibility of gold (III)-Mediated regenerated and thiolated silk fibroin hydrogels. Biomolecules 10, 466. https://doi.org/10.3390/biom10030466.

Li, J., Li, B., Liu, M., 2019. One-step synthesis of mannose-modified polyethyleneimine copolymer particles as fluorescent probes for the detection of Escherichia coli. Sensor. Actuator. B Chem. 280, 171–176. https://doi.org/10.1016/j.snb.2018.10.018.

Lu, M., Cao, C., Wang, F., Liu, G., 2021. A polyethyleneimine reduced graphene oxide/gold nanocubes based electrochemical aptasensor for chloramphenicol detection using single-stranded DNA-binding protein. Mater. Des. 199, 109409 https://doi.org/10.1016/j.matdes.2020.109409.

MOST WIEDZY Downloaded from mostwiedzy.pl

Merli, P., Furnari, R., Fadda, M., De Francesco, A., McConnell, R., Massazza, G., 2020. Role of bioelectrical impedance analysis in the evaluation of patients with upper limb lymphedema. Lymphatic Res. Biol. 18, 555–559. https://doi.org/10.1089/lrb.2019.0085.

Meunier, A., Triffaux, E., Bizzotto, D., Buess-Herman, C., Doneux, T., 2015. In situ fluorescence microscopy study of the interfacial inhomogeneity of DNA mixed self-assembled monolayers at gold electrodes. Chemelectrochem 2, 434–442. https://doi.org/10.1002/celc.201402273.

Murillo-Ortiz, B., Hernández-Ramírez, A., Rivera-Villanueva, T., Suárez-García, D., Murguía-Pérez, M., Martínez-Garza, S., Rodríguez-Penin, A., Romero-Coripuna, R., López-Partida, X.M., 2020. Monofrequency electrical impedance mammography (EIM) diagnostic system in breast cancer screening. BMC Cancer 20, 876. https://doi.org/10.1186/s12885-020-07283-5.

Nicolle, L.E., Gupta, K., Bradley, S.F., Colgan, R., DeMuri, G.P., Drekonja, D., Eckert, L. O., Geerlings, S.E., Köves, B., Hooton, T.M., Juthani-Mehta, M., Knight, S.L., Saint, S., Schaeffer, A.J., Trautner, B., Wullt, B., Siemieniuk, R., 2019. Clinical practice guideline for the management of asymptomatic bacteriuria: 2019 update by the infectious diseases society of americaa. Clin. Infect. Dis. https://doi.org/10.1093/cid/ciy1121.

Niedzialkowski, P., Koterwa, A., Olejnik, A., Zielinski, A., Gornicka, K., Brodowski, M., Bogdanowicz, R., Ryl, J., 2022. Deciphering the molecular mechanism of substrate-induced assembly of gold nanocube arrays toward an accelerated electrocatalytic effect employing heterogeneous diffusion field confinement. Langmuir 38, 9597–9610. https://doi.org/10.1021/acs.langmuir.2c01001.

Niedzialkowski, P., Slepski, P., Wysocka, J., Chamier-Cieminska, J., Burczyk, L., Sobaszek, M., Wcislo, A., Ossowski, T., Bogdanowicz, R., Ryl, J., 2020. Multisine impedimetric probing of biocatalytic reactions for label-free detection of DEFB1 gene: how to verify that your dog is not human? Sensor. Actuator. B Chem. 323, 128664 https://doi.org/10.1016/j.snb.2020.128664.

Olanrewaju, A.O., Ng, A., DeCorwin-Martin, P., Robillard, A., Juncker, D., 2017. Microfluidic capillaric circuit for rapid and facile bacteria detection. Anal. Chem. 89, 6846–6853. https://doi.org/10.1021/acs.analchem.7b01315.

Pandey, C.M., Tiwari, I., Singh, V.N., Sood, K.N., Sumana, G., Malhotra, B.D., 2017. Highly sensitive electrochemical immunosensor based on graphene-wrapped copper oxide-cysteine hierarchical structure for detection of pathogenic bacteria. Sensor. Actuator. B Chem. 238, 1060–1069. https://doi.org/10.1016/j.snb.2016.07.121.

Park, J.-E., Lee, Y., Nam, J.-M., 2018. Precisely shaped, uniformly formed gold nanocubes with ultrahigh reproducibility in single-particle scattering and surface-enhanced Raman scattering. Nano Lett. 18, 6475–6482. https://doi.org/10.1021/acs.nanolett.8b02973.

Passiu, C., Rossi, A., Weinert, M., Tysoe, W., Spencer, N.D., 2020. Probing the outermost layer of thin gold films by XPS and density functional theory. Appl. Surf. Sci. 507, 145084 https://doi.org/10.1016/j.apsusc.2019.145084.

Pierpaoli, M., Lewkowicz, A., Dec, B., Nadolska, M., Bogdanowicz, R., 2022. Impedimetric sensing of α-amino acids driven by micro-patterned 1,8-Diazafluoren-9-one into titania- boron- doped maze-like nanocarbons. Sensor. Actuator. B Chem. 371, 132459 https://doi.org/10.1016/j.snb.2022.132459.

Price, T.K., Dune, T., Hilt, E.E., Thomas-White, K.J., Kliethermes, S., Brincat, C., Brubaker, L., Wolfe, A.J., Mueller, E.R., Schreckenberger, P.C., 2016. The clinical urine culture: enhanced techniques improve detection of clinically relevant microorganisms. J. Clin. Microbiol. 54, 1216–1222. https://doi.org/10.1128/JCM.00044-16.

Qu, J., Yuan, Z., Wang, C., Wang, A., Liu, X., Wei, B., Wen, Y., 2019. Enhancing the redispersibility of TEMPO-mediated oxidized cellulose nanofibrils in N,N-dimethylformamide by modification with cetyltrimethylammonium bromide. Cellulose 26, 7769–7780. https://doi.org/10.1007/s10570-019-02655-y.

Raj, P., Oh, M.H., Han, K., Lee, T.Y., 2021. Label-Free electrochemical biosensor based on Au@MoS₂–PANI for Escherichia coli detection. Chemosensors 9, 49. https://doi.org/10.3390/chemosensors9030049.

Romero Coripuna, R.L., Hernandez Farias, D.I., Murillo Ortiz, B.O., Padierna, L.C., Fraga, T.C., 2021. Machine learning for the analysis of conductivity from mono frequency electrical impedance mammography as a breast cancer risk factor. IEEE Access 9, 152397–152407. https://doi.org/10.1109/ACCESS.2021.3122948.

Russo, M.J., Han, M., Desroches, P.E., Manasa, C.S., Dennaoui, J., Quigley, A.F., Kapsa, R.M.I., Moulton, S.E., Guijt, R.M., Greene, G.W., Silva, S.M., 2021. Antifouling strategies for electrochemical biosensing: mechanisms and performance toward point of care based diagnostic applications. ACS Sens. 6, 1482–1507. https://doi.org/10.1021/acssensors.1c00390.

Safavieh, M., Ahmed, M.U., Tolba, M., Zourob, M., 2012. Microfluidic electrochemical assay for rapid detection and quantification of Escherichia coli. Biosens. Bioelectron. 31, 523–528. https://doi.org/10.1016/j.bios.2011.11.032.

Sarigul, N., Korkmaz, F., Kurultak, İ., 2019. A new artificial urine protocol to better imitate human urine. Sci. Rep. 9, 20159 https://doi.org/10.1038/s41598-019-56693-4.

Settu, K., Chen, C.-J., Liu, J.-T., Chen, C.-L., Tsai, J.-Z., 2015. Impedimetric method for measuring ultra-low E. coli concentrations in human urine. Biosens. Bioelectron. 66, 244–250. https://doi.org/10.1016/j.bios.2014.11.027.

Shah Utsav, S., Subramaniam, V., Tamhankar Ashwin, S., 2021. Microbiome studies in urology- where do we stand and where can we reach? Indian J. Med. Microbiol. 39, 98–103. https://doi.org/10.1016/j.ijmmb.2020.10.009.

Shahrokhian, S., Ranjbar, S., 2018. Aptamer immobilization on amino-functionalized metal–organic frameworks: an ultrasensitive platform for the electrochemical diagnostic of *Escherichia coli O157:H7*. Analyst 143, 3191–3201. https://doi.org/10.1039/C8AN00725J.

Sharifi, M., Avadi, M.R., Attar, F., Dashtestani, F., Ghorchian, H., Rezayat, S.M., Saboury, A.A., Falahati, M., 2019. Cancer diagnosis using nanomaterials based electrochemical nanobiosensors. Biosens. Bioelectron. 126, 773–784. https://doi.org/10.1016/j.bios.2018.11.026.

Shoaie, N., Forouzandeh, M., Omidfar, K., 2018. Voltammetric determination of the Escherichia coli DNA using a screen-printed carbon electrode modified with polyaniline and gold nanoparticles. Microchim. Acta 185, 217. https://doi.org/10.1007/s00604-018-2749-y.

Silva-Moraes, M.O., Garcia-Basabe, Y., de Souza, R.F.B., Mota, A.J., Passos, R.R., Galante, D., Fonseca Filho, H.D., Romaguera-Barcelay, Y., Rocco, M.L.M., Brito, W. R., 2018. Geometry-dependent DNA-TiO2 immobilization mechanism: a spectroscopic approach. Spectrochim. Acta Mol. Biomol. Spectrosc. 199, 349–355. https://doi.org/10.1016/j.saa.2018.03.081.

Singhal, C., Dubey, A., Mathur, A., Pundir, C.S., Narang, J., 2018. Paper based DNA biosensor for detection of chikungunya virus using gold shells coated magnetic nanocubes. Process Biochem. 74, 35–42. https://doi.org/10.1016/j.procbio.2018.08.020.

Sun, Q., Yan, F., Yao, L., Su, B., 2016. Anti-biofouling isoporous silica-micelle membrane enabling drug detection in human whole blood. Anal. Chem. 88, 8364–8368. https://doi.org/10.1021/acs.analchem.6b02091.

Van Stralen, K.J., Stel, V.S., Reitsma, J.B., Dekker, F.W., Zoccali, C., Jager, K.J., 2009. Diagnostic methods I: sensitivity, specificity, and other measures of accuracy. Kidney Int. 75, 1257–1263. https://doi.org/10.1038/ki.2009.92.

Velayudham, J., Magudeeswaran, V., Paramasivam, S.S., Karruppaya, G., Manickam, P., 2021. Hydrogel-aptamer nanocomposite based electrochemical sensor for the detection of progesterone. Mater. Lett. 305, 130801 https://doi.org/10.1016/j.matlet.2021.130801.

Vitale, F., Fratoddi, I., Battocchio, C., Piscopiello, E., Tapfer, L., Russo, M.V., Polzonetti, G., Giannini, C., 2011. Mono- and bi-functional arenethiols as surfactants for gold nanoparticles: synthesis and characterization. Nanoscale Res. Lett. 6, 103. https://doi.org/10.1186/1556-276X-6-103.

Wang, H., Zhao, Y., Bie, S., Suo, T., Jia, G., Liu, B., Ye, R., Li, Z., 2019. Development of an electrochemical biosensor for rapid and effective detection of pathogenic Escherichia coli in licorice extract. Appl. Sci. 9, 295. https://doi.org/10.3390/app9020295.

Wang, J., 2015. Design and Implementation of an Impedance Analyzer Based on Arduino Uno.

Wang, R., Lum, J., Callaway, Z., Lin, J., Bottje, W., Li, Y., 2015. A label-free impedance immunosensor using screen-printed interdigitated electrodes and magnetic nanobeads for the detection of E. coli O157:H7. Biosensors 5, 791–803. https://doi.org/10.3390/bios5040791.

Wang, Y., Fewins, P.A., Alocilja, E.C., 2015. Electrochemical immunosensor using nanoparticle-based signal enhancement for Escherichia coli O157:H7 detection. IEEE Sensor. J. 15, 4692–4699. https://doi.org/10.1109/JSEN.2015.2396036.

Wu, J.-J., 2010. The jump-to-contact distance in atomic force microscopy measurement. J. Adhes. 86, 1071–1085. https://doi.org/10.1080/00218464.2010.519256.

Wu, S., Su, F., Dong, X., Ma, C., Pang, L., Peng, D., Wang, M., He, L., Zhang, Z., 2017. Development of glucose biosensors based on plasma polymerization-assisted nanocomposites of polyaniline, tin oxide, and three-dimensional reduced graphene oxide. Appl. Surf. Sci. 401, 262–270. https://doi.org/10.1016/j.apsusc.2017.01.024.

Xiao, T., Huang, J., Wang, D., Meng, T., Yang, X., 2020. Au and Au-Based nanomaterials: synthesis and recent progress in electrochemical sensor applications. Talanta 206, 120210. https://doi.org/10.1016/j.talanta.2019.120210.

Xu, J., Hong, Z., 2022. Low power bio-impedance sensor interfaces: review and electronics design methodology. IEEE Rev. Biomed. Eng. 15, 23–35. https://doi.org/10.1109/RBME.2020.3041053.

Xu, M., Wang, R., Li, Y., 2016. Rapid detection of Escherichia coli O157:H7 and Salmonella Typhimurium in foods using an electrochemical immunosensor based on screen-printed interdigitated microelectrode and immunomagnetic separation. Talanta 148, 200–208. https://doi.org/10.1016/j.talanta.2015.10.082.

Yang, D., Wang, J., Cao, Y., Tong, X., Hua, T., Qin, R., Shao, Y., 2023. Polyaniline-based biological and chemical sensors: sensing mechanism, configuration design, and perspective. ACS Appl. Electron. Mater. 5, 593–611. https://doi.org/10.1021/acsaelm.2c01405.

Zhou, M., Zhai, Y., Dong, S., 2009. Electrochemical sensing and biosensing platform based on chemically reduced graphene oxide. Anal. Chem. 81, 5603–5613. https://doi.org/10.1021/ac900136z.

MOST WIEDZY Downloaded from mostwiedzy.pl